
DISENTANGLED SEQUENCE CLUSTERING FOR HUMAN INTENTION INFERENCE

Mark Zolotas*

Dept. of Electrical and Electronic Engineering
Imperial College London
SW7 2BT, UK
mark.zolotas12@imperial.ac.uk

Yiannis Demiris

Dept. of Electrical and Electronic Engineering
Imperial College London
SW7 2BT, UK
y.demiris@imperial.ac.uk

ABSTRACT

Equipping robots with the ability to infer human intent is a vital precondition for effective collaboration. Most computational approaches towards this objective derive a probabilistic distribution of “intent” conditioned on the robot’s perceived sensory state. However, these approaches typically assume task-specific labels of human intent are known *a priori*. To overcome this constraint, we propose the Disentangled Sequence Clustering Variational Autoencoder (DiSCVAE), a clustering framework capable of learning such a distribution of intent in an *unsupervised* manner. The DiSCVAE leverages recent advances in unsupervised learning to recover a disentangled latent representation of sequential data, separating time-varying local features from time-invariant global aspects. Though unlike previous frameworks for disentanglement, the proposed variant also infers a discrete variable to form a latent mixture model and enable clustering of global sequence concepts, *e.g.* intentions from observed human behaviour. To evaluate the DiSCVAE, we first validate its capacity to discover classes from unlabelled sequences using video datasets of bouncing digits and 2D animations. We then report results from a real-world human-robot interaction experiment conducted on a robotic wheelchair. Our findings reveal that the inferred discrete variable coincides with human intent and can thus improve assistance in collaborative settings, such as shared control.

Keywords Human Intention Inference · Unsupervised Clustering · Learning in Robotics · Deep Generative Models

1 Introduction

Humans are remarkably proficient at accurately and rapidly inferring the implicit intentions of others from their overt behaviour [1, 2]. Consequently, humans are adept at planning their own actions when collaborating with each other. It therefore stands to reason that intention inference may be equally imperative in creating fluid and effective human-robot collaborations. Robots endowed with this ability have been extensively explored [3–5], yet their integration into real-world settings remains an open research problem.

One major impediment to real-world instances of robots inferring human intent is the assumption that a known representation of intent exists. For example, most prevalent frameworks in collaborative robotics assume a discrete set of task goals is known *a priori*. Under this assumption, the robot can infer a distribution of human intent by applying Bayesian reasoning over the entire goal space [5–7]. Whilst such a distribution offers a versatile and practical representation of intent, the need for predefined labels to acquire it is not always feasible or realistic unless restricted to a specific task scope [8].

Another fundamental challenge is that many diverse actions often fulfil the same intention. A popular class of probabilistic algorithms for overcoming this challenge are generative models, which derive a distribution of observations by introducing latent random variables to capture any hidden underlying structure. Within the confines of intention inference, the modelled latent space is then presumed to represent all possible causal relations between intentions and observed human behaviour [9–11]. The advent of deep generative models, such as Variational Autoencoders

*Corresponding author

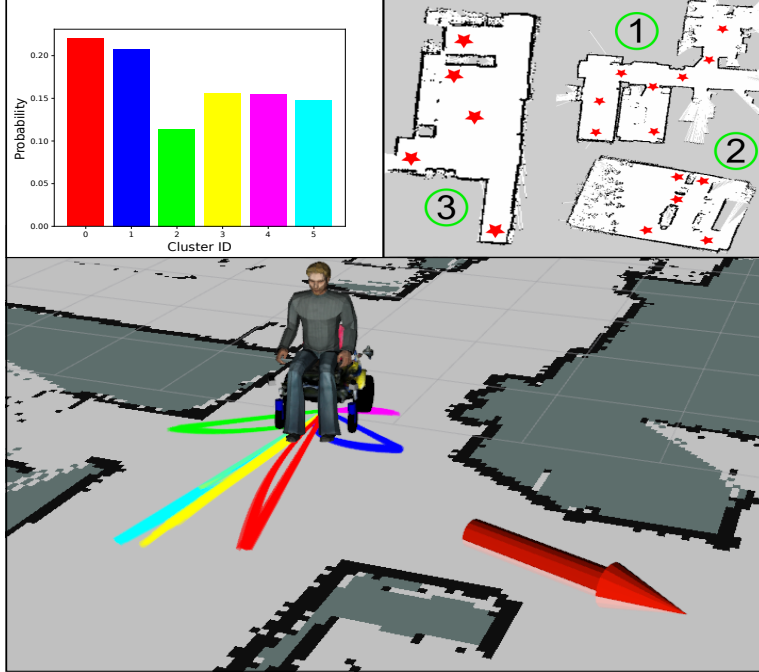


Figure 1: Overview of the intention inference experiment on a robotic wheelchair (see Fig. 7 for the real robot platform). **Bottom:** Recorded output of an *actual* human subject navigating towards a goal (red arrow), which is visualised here as an animated simulation. **Top Right:** Maps of the three experiment settings, with red stars denoting target locations. **Top Left:** Probability histogram of the categorical variable modelling “intentions” at this particular snapshot of the data for $K = 6$ clusters. The bars are coloured to align with the wheelchair trajectories generated by sampling from the corresponding clusters. Multiple diverse trajectories can be sampled from the same cluster and each trajectory’s length is dependent on the velocity commands drawn from the generative model. Figure best viewed in colour.

(VAEs) [12, 13], has also made it possible to efficiently infer this latent space from abundant sources of highly complex data.

Inspired by the prospects of not only extracting hidden “intent” variables but also interpreting their meaning, we frame the intention inference problem as a process of *disentangling* the latent space. Disentanglement is a core research thrust in representation learning that refers to the recovery of abstract concepts from independent factors of variation assumed to be responsible for generating the observed data [14, 15]. These independent factors could be the handwriting style of digits in the MNIST dataset [16], or the orientation and motion of objects in videos [17–21], or even the speaker identity in audio signals [22–24]. The interpretable structure of such disentangled representations is exceedingly desirable for human-in-the-loop scenarios [25], like robotic wheelchair assistance, however few applications have transferred over to the robotics domain [11].

We strive to bridge this gap by proposing an *unsupervised* disentanglement framework suitable for human intention inference. Capitalising on prior disentanglement techniques, we learn a latent representation of sequence observations that divides into a local (time-varying) and global (time-preserving) part [17–22]. Our proposed variant simultaneously infers a categorical variable to construct a mixture model and thereby form clusters in the global latent space. In the scope of intention inference, we view the local *continuous* variable space as representative of desirable low-level trajectories (*e.g.* control commands), whilst the global *discrete* counterpart signifies high-level intentions (*e.g.* navigation manoeuvres).

In summary, the main contributions of this paper are:

- A framework for clustering disentangled representations of sequences, coined as the *Disentangled Sequence Clustering Variational Autoencoder (DiSCVAE)*;
- An evaluation of how the DiSCVAE performs at unsupervised classification and structured prediction on the Moving MNIST [26] and Sprites datasets [20];

- Findings from a human-robot interaction experiment involving a robotic wheelchair (see Fig. 1), which demonstrate how clusters *interpretable* as intent are learnt without explicit supervision, or strongly correlate to “labels” of intent in a semi-supervised context.

The paper is organised as follows. In Section 2, we describe the preliminary material supporting our DiSCVAE and then define it in Section 3. Experimental results of the proposed method applied to the Moving MNIST, Sprites and robotic wheelchair domains are presented in Sections 4, 5 and 6, respectively. Section 7 discusses related ideas on deep generative models, disentanglement and intention estimation. Finally, Section 8 concludes with the implications of this work on future research in human-robot interaction.

2 Preliminaries

The following describes principles from representation learning that underpin our clustering framework. Given that the VAE acts as the basis of this framework, we begin with a brief overview of its foundations. We then examine how to tailor VAEs to sequential data, as they are not directly suitable for time series analysis in their original form.

2.1 Variational Autoencoder (VAE)

Deep generative models are density estimators of data that rely on neural networks to predict probability distribution parameters. In this context, the joint distribution $p_\theta(\mathbf{x}, \mathbf{z})$ is acquired by drawing latent variables \mathbf{z} from a prior $p(\mathbf{z})$ and reproducing observations \mathbf{x} from a non-linear likelihood function $p_\theta(\mathbf{x} | \mathbf{z})$ with parameters θ output from a *generative network*. Though for Bayesian inference, the sought-after posterior $p(\mathbf{z} | \mathbf{x})$ is often intractable when using such a non-linear functional mapping. To bypass this problem, a mean-field approximation of the posterior as a factorised distribution over all data points $q_\phi(\mathbf{z} | \mathbf{x})$ is instead computed, where parameters ϕ are learnt via a *recognition network* [12, 13].

The VAE is thus a deep latent variable model (displayed in Fig. 2a) that consists of a generative and recognition network. These networks can be jointly trained by applying the reparameterisation trick [12, 13] and maximising the evidence lower bound (ELBO) $\mathcal{L}(\mathbf{x}; \theta, \phi)$ on the marginal log-likelihood:

$$\begin{aligned} \log p_\theta(\mathbf{x}) &\geq \mathcal{L}(\mathbf{x}; \theta, \phi) \\ &\equiv \mathbb{E}_{q_\phi(\mathbf{z} | \mathbf{x})} [\log p_\theta(\mathbf{x} | \mathbf{z})] - \text{KL}(q_\phi(\mathbf{z} | \mathbf{x}) || p(\mathbf{z})), \end{aligned} \tag{1}$$

where the first term can be viewed as the reconstruction error and the second Kullback-Leibler (KL) divergence term as a regulariser that encourages the variational posterior $q_\phi(\mathbf{z} | \mathbf{x})$ to be close to the prior $p_\theta(\mathbf{z})$. For notational simplicity, parameters ϕ and θ will be omitted hereafter.

2.2 Variational Inference for Sequences

Most real-world data are characterised by time-varying attributes, motivating the development of deep generative models for sequences. Nevertheless, the multi-layered structure of sequence data is a challenging modelling task where variables at different timesteps are highly correlated and cannot be assumed independent as in the factorised variational distribution of a VAE. In order to explicitly capture these correlations, a recurrence relationship must be established between the internal states of the latent variable model.

State space models (SSMs), such as Hidden Markov Models (HMMs), accomplish this feat using structured variational inference. The structured qualifier denotes how the variational approximation *directly* models dependencies between *stochastic* units, rather than factor them out [27]. Regardless of the rich history behind SSMs, they have only recently been merged with deep neural networks to leverage the expressive power of Recurrent Neural Networks (RNNs) for sequence learning [28, 29]. Deep SSMs are therefore latent variable models composed of structured inference (or recognition) networks parameterised by RNNs and optimised in line with the VAE learning principle.

Alternatively, RNNs can be augmented to include latent variables and model connections between *deterministic* states. By persisting the recurrent connections of hidden states with themselves, the RNN retains its autoregressive nature. A notable example is the Variational Recurrent Neural Network (VRNN) [30] (shown in Fig. 2b), which differs from SSMs by *indirectly* conditioning on random variables and observations from previous timesteps through the deterministic hidden state, $\mathbf{h}_t(\mathbf{x}_{t-1}, \mathbf{z}_{t-1}, \mathbf{h}_{t-1})$. This leads to a joint distribution over the observation sequence and latent

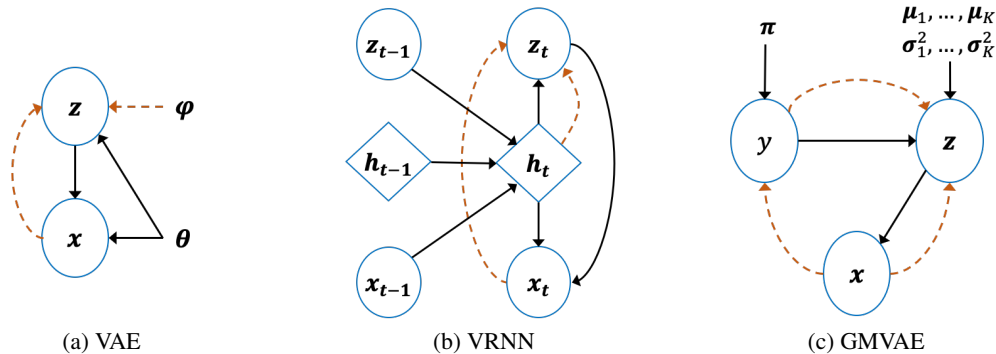


Figure 2: Deep generative models for: (a) variational inference [12, 13]; (b) a sequential VAE that conditions on the deterministic hidden states of an RNN at each timestep (VRNN [30]); (c) a VAE with a Gaussian mixture prior (GMVAE). Dashed lines denote inference and bold lines indicate generation.

states:

$$\begin{aligned}
 p(\mathbf{x}_{\leq T}, \mathbf{z}_{\leq T}) &= \prod_{t=1}^T p(\mathbf{x}_t | \mathbf{z}_{\leq t}, \mathbf{x}_{<t}) p(\mathbf{z}_t | \mathbf{x}_{<t}, \mathbf{z}_{<t}) \\
 &= \prod_{t=1}^T p(\mathbf{x}_t | \mathbf{z}_t, \mathbf{h}_t) p(\mathbf{z}_t | \mathbf{h}_t),
 \end{aligned} \tag{2}$$

where the true posterior is conditioned on information pertaining to previous observations $\mathbf{x}_{<t}$ and latent states $\mathbf{z}_{<t}$, hence accounting for temporal dependencies. The VRNN state \mathbf{h}_t is also shared with the inference procedure to yield the following variational posterior distribution:

$$q(\mathbf{z}_{\leq T} | \mathbf{x}_{\leq T}) = \prod_{t=1}^T q(\mathbf{z}_t | \mathbf{x}_{\leq t}, \mathbf{z}_{<t}) = \prod_{t=1}^T q(\mathbf{z}_t | \mathbf{x}_t, \mathbf{h}_t). \tag{3}$$

Deciding how to incorporate stochastic variables into a recurrent model is an architecture choice [27, 31]. Whilst deep SSMs [28, 29] provide a tighter ELBO than that of a VRNN, they lose autoregressive structure by not conditioning on the deterministic hidden state [31]. A recent framework aiming to unify several of these architecture choices emphasised the benefit of indirectly conditioning on stochastic latent variables to encode a “plan” about future states during inference [31]. As our preliminary results resonated with these findings, the DiSCVAE also elects an approach akin to a VRNN [30].

3 The Disentangled Sequence Clustering Variational Autoencoder

In this section, we introduce the *Disentangled Sequence Clustering VAE (DiSCVAE)*², a probabilistic framework suited for human intention inference. Clustering is initially presented as an adaptation of the VAE to incorporate a Gaussian mixture prior and a categorical variable. We then formulate the DiSCVAE by combining clustering with a sequential latent variable model for disentanglement. Finally, we relate back to the intention inference domain.

3.1 Clustering with Variational Autoencoders

A key element of learning “good” representations through generative models is expressing a prior capable of naturally clustering data [14]. Previous research on VAEs has pursued this objective by segmenting the latent space into distinct classes using a Gaussian mixture prior instead of the standard unimodal Gaussian [32, 33], *i.e.* a GMVAE.

Our approach is similar to earlier GMVAEs, except for two modifications from recent literature. First, we leverage the categorical reparameterisation trick [34, 35] to obtain differentiable samples of *discrete* variables, thereby enabling gradient descent for model optimisation. Second, we alter the ELBO objective to mitigate the precarious issues of

²Code available at: <https://github.com/mazrk7/discvae>

posterior collapse and cluster degeneracy (mode collapse) [36]. Posterior collapse refers to the phenomenon of latent variables being ignored or overpowered by highly expressive decoders during training, such that the posterior mimics the prior, *i.e.* the KL divergence term in Eq. 1 falls to zero [24, 37]. On the other hand, when multiple modes of the prior have collapsed into one, then this indicates cluster degeneracy [23, 32, 36].

The GMVAE used for this work (see Fig. 2c) is outlined below. Assuming observations \mathbf{x} are generated according to some stochastic process with a discrete latent variable y and a continuous latent variable \mathbf{z} , and that the aim is to divulge K clusters, then we can write the joint probability as:

$$\begin{aligned} p(\mathbf{x}, \mathbf{z}, y) &= p(\mathbf{x} | \mathbf{z})p(\mathbf{z} | y)p(y) & (4) \\ y &\sim \text{Cat}(\boldsymbol{\pi}) \\ \mathbf{z} &\sim \mathcal{N}(\boldsymbol{\mu}_z(y), \text{diag}(\boldsymbol{\sigma}_z^2(y))) \\ \mathbf{x} &\sim \mathcal{N}(\boldsymbol{\mu}_x(\mathbf{z}), \mathbf{I}) \text{ or } \mathcal{B}(\boldsymbol{\mu}_x(\mathbf{z})), \end{aligned}$$

where functions $\boldsymbol{\mu}_z$, $\boldsymbol{\sigma}_z^2$ and $\boldsymbol{\mu}_x$ are neural networks whose outputs parameterise the distributions of \mathbf{z} and \mathbf{x} . More specifically, the generative process involves three steps: (1) sampling y from categorical distribution $\text{Cat}(y | \boldsymbol{\pi})$ parameterised by probability vector $\boldsymbol{\pi}$, with π_k set to K^{-1} in favour of an uninformative uniform prior; (2) sampling \mathbf{z} from the marginal prior $p(\mathbf{z} | y)$, resulting in a Gaussian mixture model (GMM) with a diagonal covariance matrix and uniform mixture weights; and (3) generating data \mathbf{x} from a likelihood function $p(\mathbf{x} | \mathbf{z})$, *e.g.* a fixed unit variance Gaussian if real-valued (\mathbf{I} denoting the identity matrix) or a Bernoulli if binary.

A mean-field approximation $q(\mathbf{z}, y | \mathbf{x})$ of the true posteriors on \mathbf{z} and y is introduced in its factorised form as:

$$q(\mathbf{z}, y | \mathbf{x}) = q(\mathbf{z} | \mathbf{x}, y)q(y | \mathbf{x}), \quad (5)$$

where both the normally distributed $q(\mathbf{z} | \mathbf{x}, y)$ and categorical $q(y | \mathbf{x})$ are also parameterised by neural networks. Nonetheless, the standard reparameterisation trick does not directly apply to the non-differentiable case of discrete samples [12, 13]. Instead, we employ a continuous relaxation of $q(y | \mathbf{x})$ during training, coined as the Concrete [34] or Gumbel-Softmax [35] distribution³. This enables efficient training of our hybrid model, removing the need to marginalise over all K class values [35].

The ELBO for this clustering model is:

$$\begin{aligned} \mathcal{L}(\mathbf{x}) &= \mathbb{E}_{q(\mathbf{z}, y | \mathbf{x})} \left[\log \frac{p(\mathbf{x}, \mathbf{z}, y)}{q(\mathbf{z}, y | \mathbf{x})} \right] & (6) \\ &= \mathbb{E}_{q(\mathbf{z} | \mathbf{x}, y)} [\log p(\mathbf{x} | \mathbf{z})] \\ &\quad - \mathbb{E}_{q(y | \mathbf{x})} [\text{KL}(q(\mathbf{z} | \mathbf{x}, y) || p(\mathbf{z} | y))] \\ &\quad - \text{KL}(q(y | \mathbf{x}) || p(y)), \end{aligned}$$

where the first term acts as a reconstruction loss on observations \mathbf{x} , and the latter two terms push the variational posteriors close to their corresponding priors.

Optimising the ELBO for GMVAEs with powerful decoders is prone to posterior collapse and mode collapse. Cluster degeneracy is particularly problematic for $p(\mathbf{z} | y)$, where the KL divergence term on y opts to use the same mean and variance for each mixture component [23, 32]. To prevent these negative outcomes, we exploit a known relationship to mutual information $I(y; \mathbf{x})$ between y and \mathbf{x} [38–40]:

$$\begin{aligned} \mathbb{E}_{p(\mathbf{x})} [\text{KL}(q(y | \mathbf{x}) || p(y))] &= I(y; \mathbf{x}) + \text{KL}(q(y) || p(y)) \\ &\geq I(y; \mathbf{x}) \equiv \mathcal{H}(y) - \mathcal{H}(y | \mathbf{x}) \\ &= \log K - \mathcal{H}(y | \mathbf{x}). \end{aligned} \quad (7)$$

Provided that $p(y)$ is uniform, directly maximising the entropy on $q(y | \mathbf{x})$ is equivalent to minimising a mini-batch estimate of $\text{KL}(q(y | \mathbf{x}) || p(y))$. As with previous VAE-based clustering models [23, 36], we make this replacement in Eq. 6 to alleviate posterior collapse and impose a constraint that specialises clusters to individual observations. Empirical evidence supporting this argument is supplied in Section 4.4.

3.2 Model Specification

Having established a way of categorising the VAE latent space learnt over static data, we now derive the DiSCVAE as a sequential extension (graphically shown in Fig. 3). The motivation behind our proposed framework is to automatically

³In practice, a continuous relaxation of a one-hot categorical distribution is utilised, such that samples from $q(y | \mathbf{x})$ are one-hot vectors.

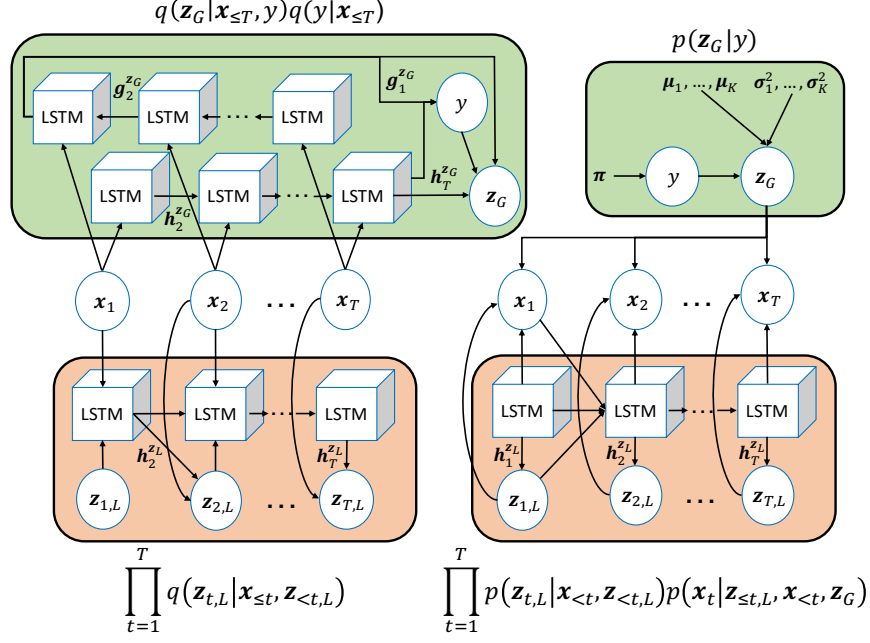


Figure 3: Computation graph of the inference $q(\cdot)$ and generative $p(\cdot)$ networks. **Green** blocks contain global variables y and \mathbf{z}_G , with a bidirectional LSTM conditioning over input sequence $\mathbf{x}_{\leq T}$. Hidden states $\mathbf{h}_t^{\mathbf{z}_G}$ and $\mathbf{g}_1^{\mathbf{z}_G}$ then compute the $q(\cdot)$ distribution parameters. **Orange** blocks encompass the local sequence variable $\mathbf{z}_{t,L}$, where the internal states $\mathbf{h}_t^{\mathbf{z}_L}$ of an LSTM cell are combined at each timestep with current inputs \mathbf{x}_t to infer $\mathbf{z}_{t,L}$. Generating \mathbf{x}_t requires *both* \mathbf{z}_G and $\mathbf{z}_{t,L}$. Figure best viewed in colour.

disentangle representations and cluster them into meaningful classes of information. In doing so, we aim to preserve the predictive benefits of autoregressive latent variable models, as well as boost model *interpretability* via controlled generation.

Disentangling latent variables has recently gained traction in deep generative models for sequences [17–23]. A common choice of disentanglement amongst these models involves segregating into *time-invariant* and *time-dependent* subsets [15]. This can generally be regarded as splitting latent attributes into two parts, *e.g.* sequence-level and segment-level [22], static and dynamic [20, 21], or content and motion [17–19]. Similarly, we specify our disentangled representation of input sequence $\mathbf{x}_{\leq T}$ at timestep t as $\mathbf{z}_t = [\mathbf{z}_G, \mathbf{z}_{t,L}]$, where \mathbf{z}_G and $\mathbf{z}_{t,L}$ encode *global* and *local* characteristics.

The novelty of our approach lies in how we solely cluster the global (time-invariant) variable \mathbf{z}_G extracted from sequences. Temporal clustering models related to ours have either mapped the entire sequence $\mathbf{x}_{\leq T}$ to a discrete latent manifold [25] or inferred a categorical factor of variation y to cluster over an *entangled* continuous latent representation [23, 36]. Whereas the DiSCVAE clusters high-level attributes \mathbf{z}_G in isolation from lower-level dynamics $\mathbf{z}_{t,L}$. The DiSCVAE model itself is an amalgamation of prior works (*e.g.* the VRNN [30], GMVAEs [32, 33] and sequence disentanglement [20]), however its formulation plays a symbolic role in our interpretation of intention inference, as is made apparent in Section 3.4.

Using the clustering scheme described in Section 3.1, we define the generative model $p(\mathbf{x}_{\leq T}, \mathbf{z}_{\leq T,L}, \mathbf{z}_G, y)$ as:

$$p(\mathbf{z}_G | y)p(y) \prod_{t=1}^T p(\mathbf{x}_t | \mathbf{z}_{t,L}, \mathbf{z}_G, \mathbf{h}_t^{\mathbf{z}_L})p(\mathbf{z}_{t,L} | \mathbf{h}_t^{\mathbf{z}_L}). \quad (8)$$

The GMM prior $p(\mathbf{z}_G | y)$ encourages mixture components (indexed by y) to emerge in the latent space of variable \mathbf{z}_G . Akin to a VRNN [30], the posterior of $\mathbf{z}_{t,L}$ is parameterised by deterministic state $\mathbf{h}_t^{\mathbf{z}_L}$. We also highlight the dependency on both $\mathbf{z}_{t,L}$ and \mathbf{z}_G upon generating \mathbf{x}_t .

To perform posterior approximation, we adopt the variational distribution $q(\mathbf{z}_{\leq T,L}, \mathbf{z}_G, y | \mathbf{x}_{\leq T})$ and factorise it as:

$$q(\mathbf{z}_G | \mathbf{x}_{\leq T}, y)q(y | \mathbf{x}_{\leq T}) \prod_{t=1}^T q(\mathbf{z}_{t,L} | \mathbf{x}_t, \mathbf{h}_t^{\mathbf{z}_L}), \quad (9)$$

Algorithm 1: Sampling to produce diverse predictions of goal states from the inferred cluster c

Input: Observation sequence $\mathbf{x}_{\leq t}$; sample length L ;

Output: Predicted states $\tilde{\mathbf{x}}_{t+1}, \dots, \tilde{\mathbf{x}}_{t+L}$

Feed prefix $\mathbf{x}_{\leq t}$ into inference model (Eq. 9)

Infer cluster c using Eq. 11

Draw fixed global sample from $p(\mathbf{z}_G | y = c)$

for $i \in \{t + 1, \dots, t + L\}$ **do**

Update $\mathbf{h}_i \leftarrow \text{RNN}(\mathbf{z}_{i-1}, \mathbf{x}_{i-1}, \mathbf{h}_{i-1})$

Sample local dynamics from $p(\mathbf{z}_{i,L} | \mathbf{h}_i)$

Predict $\tilde{\mathbf{x}}_i \sim p(\mathbf{x}_i | \mathbf{z}_{i,L}, \mathbf{h}_i, \mathbf{z}_G)$

end for

with relaxed categorical y injected into the process when training [34, 35]. An alternative inference process could employ a “full” structure, where the variational posterior on $\mathbf{z}_{t,L}$ also conditions on \mathbf{z}_G and y [20]. Yet we conform to a “factorised” structure under the assumption that global features are independent of local dynamics, *e.g.* a human’s high-level intention to grasp an object does not correlate with the precise intricacies of their grasping behaviour. Moreover, the variational posterior does not summarise information from the future $\mathbf{x}_{\leq T}$, as this is unlikely to render improvements given the shared deterministic state [28].

Under the VAE framework, the DiSCVAE is maximised using the time-wise objective:

$$\begin{aligned} \mathcal{L}(\mathbf{x}_{\leq T}) &= \mathbb{E}_{q(\cdot)} \left[\log \frac{p(\mathbf{x}_{\leq T}, \mathbf{z}_{\leq T,L}, \mathbf{z}_G, y)}{q(\mathbf{z}_{\leq T,L}, \mathbf{z}_G, y | \mathbf{x}_{\leq T})} \right] \\ &= \mathbb{E}_{q(\cdot)} \left[\sum_{t=1}^T \left(\log p(\mathbf{x}_t | \mathbf{z}_{t,L}, \mathbf{z}_G, \mathbf{h}_t^{\mathbf{z}_L}) \right. \right. \\ &\quad \left. \left. - \text{KL}(q(\mathbf{z}_{t,L} | \mathbf{x}_t, \mathbf{h}_t^{\mathbf{z}_L}) || p(\mathbf{z}_{t,L} | \mathbf{h}_t^{\mathbf{z}_L})) \right) \right. \\ &\quad \left. - \text{KL}(q(\mathbf{z}_G | \mathbf{x}_{\leq T}, y) || p(\mathbf{z}_G | y)) \right. \\ &\quad \left. + \mathcal{H}(q(y | \mathbf{x}_{\leq T})) \right]. \end{aligned} \tag{10}$$

This summation of lower bounds across timesteps is decomposed into: (1) the expected log-likelihood of input sequences; (2) KL divergences for variables $\mathbf{z}_{t,L}$ and \mathbf{z}_G ; and (3) a measure of conditional entropy (Eq. 7).

3.3 Network Architecture

The complete DiSCVAE network architecture is shown in Fig. 3. An RNN is used to parameterise the posteriors over $\mathbf{z}_{t,L}$, with the hidden state $\mathbf{h}_t^{\mathbf{z}_L}$ allowing $\mathbf{x}_{< t}$ and $\mathbf{z}_{< t,L}$ to be indirectly conditioned on in Eqs. 8 and 9. For time-invariant variables y and \mathbf{z}_G , a bidirectional RNN [41] extracts feature representations over the entire sequence $\mathbf{x}_{\leq T}$, analogous to prior architectures [20, 28, 29]. All RNNs have LSTM cells [42] and bidirectional outputs of the forward and reverse cells are merged by summation. One-hidden layer multilayer perceptrons (MLPs) are also dispersed throughout to output the mean and variance of any Gaussian distributions. Decoded inputs \mathbf{x}_t at each timestep depend on the concatenated disentangled representation \mathbf{z}_t .

3.4 Intention Inference

Let us now recall the problem of intention inference. We first claim that the latent class attribute y adequately models a K -dimensional repertoire of action plans when considering human interaction data for a specific task. From this perspective, intention inference is a matter of assigning clusters (or action plans) to observations $\mathbf{x}_{\leq T}$ of human behaviour and the environment (*e.g.* joystick commands and sensor data). Human intent is thus computed as the most probable element of the component posterior:

$$c = \arg \max_k q(y_k | \mathbf{x}_{\leq T}), \tag{11}$$

where c is the assigned cluster identity, *i.e.* the inferred intention label. The goal associated with this cluster is then modelled by \mathbf{z}_G , and local variable $\mathbf{z}_{t,L}$ captures the various behaviours capable of accomplishing the inferred plan.

In the robotic wheelchair scenario, most related works on intention estimation represent user intent [43, 44] as a target wheelchair state $\tilde{\mathbf{x}}_T$. Bayesian reasoning over the entire observation sequence $\mathbf{x}_{<T}$ using an entangled latent variable can yield such a state [5, 9, 10]. In contrast, the DiSCVAE employs a disentangled representation $\mathbf{z}_t = [\mathbf{z}_G, \mathbf{z}_{t,L}]$, where the goal state variable is explicitly separated from the user action and environment dynamics. The major benefit of this separation is controlled generation, where repeatedly sampling $\mathbf{z}_{t,L}$ can enable diversity in how trajectories $\tilde{\mathbf{x}}_t$ pan out according to the global plan. The procedure for inferring intention label c amongst a collection of action plans and generating diverse trajectories is summarised in Algorithm 1.

4 Validation Setting: Moving MNIST

As a means of first validating our clustering framework, this section presents results on the Moving MNIST dataset [26].

4.1 Dataset and Implementation

Moving MNIST is a video dataset [26] comprised of digits bouncing off their surrounding frame edges at random velocities. It has recently become a popular domain for investigating disentanglement amongst sequential latent variable models [18, 45] due to its intuitive division of dynamic and static sequence attributes, namely the motion and identity of each digit. The dataset is also a pertinent benchmark for the DiSCVAE, as clustering MNIST digits is a common ground for evaluation [32, 33].

Although the dataset is flexible in size given that moving digits can be rendered on-the-fly, we synthesise a fixed total of only 10000 video sequences. Not relying on an endless amount of training data offers better judgement on how our model might perform in limited data settings, *e.g.* in human-robot interaction. The 10000 sequences are split into 8000 for training, and the remaining 2000 for validation and testing. Every video is of length $T = 20$ frames, with each frame occupying a 64×64 patch. Unlike the original dataset [26], our version contains only a single 28×28 digit moving randomly within each frame, permitting $K = 10$ to be suitable for classification. Digit classes are evenly distributed across the dataset.

The DiSCVAE architecture adheres to Fig. 3. Wrapped around this architecture is a four-layer Convolutional Neural Network (CNN) to encode and decode raw video sequences. The entire network is then configured as follows: convolutional layers have 3×3 kernels and strides of two, MLP layers (leaky ReLU activations) and the bidirectional LSTM states have 512 hidden units, and the $\mathbf{h}_t^{\mathbf{z}_L}$ state shared between the inference and generative processes has 128 units. Each pixel is modelled as a Bernoulli variable represented by latent variables of dimensionality $\dim(\mathbf{z}_{t,L}) = 32$ and $\dim(\mathbf{z}_G) = 128$. The temperature parameter defining the approximate discreteness of $q(y | \mathbf{x}_{<T})$ is set to 1.0 [34, 35]. For training, we use the Adam optimiser [46] with a 3×10^{-4} learning rate and batch size of 16. We settle on these parameters through rigorous evaluation on the validation set, as hyperparameter tuning is exceptionally sensitive when learning disentangled representations [8, 39]. All functionality is implemented using TensorFlow [47] and its Probability library [48].

4.2 Evaluation Protocol

Clustering performance is determined by a frequently applied metric for unsupervised classification [33]:

$$ACC = \max_{m \in \mathcal{M}} \frac{\sum_{i=1}^N \mathbf{1}\{l_i = m(c_i)\}}{N}, \quad (12)$$

where l_i and c_i are the actual label and cluster assignment associated with observation \mathbf{x}_i , respectively. The set \mathcal{M} covers all possible one-to-one mappings between labels and learnt clusters, for which the best permutation is computed via the Hungarian linear assignment algorithm [49]. To evaluate prediction performance on Moving MNIST, the standard protocol is to sample 10 frames into the future given 10 preceding input frames, and then compare these samples with the ground truth sequence [26]. Sticking to this protocol, we report on metrics of binary cross-entropy (BCE) and mean squared error (MSE).

The following methods are considered:

- **SeqVAE-GMM:** A sequential VAE where the variables at each timestep are treated as independent of one another, plus a GMM trained afterwards on the learnt latent space;
- **SeqGMVAE:** A sequential GMVAE based on the clustering schema presented in Section 3.1, but again not handling temporal dependencies between variables;

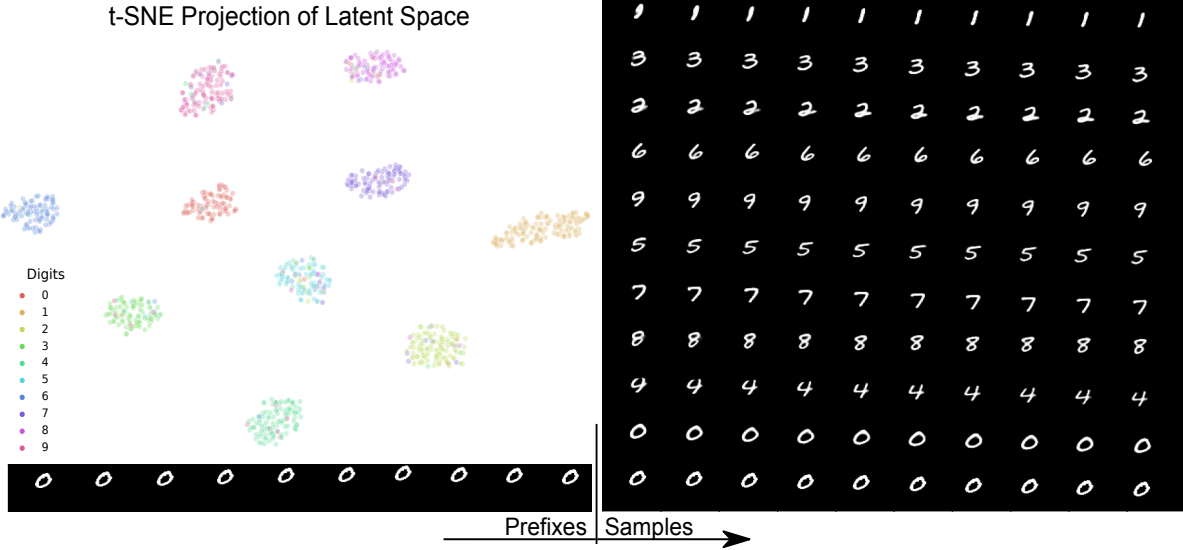


Figure 4: Bouncing digits generated by drawing samples from different mixture components. **Bottom:** Shows the ground truth sequence, where the first 10 frames prefix the sampling procedure disclosed in Algorithm 1. **Right:** Illustrates how predictions sampled from every cluster correctly persist the bouncing profile of the digit but alter its identity. The sequence just above ground truth is generated from the assigned cluster c and correctly matches the “zero” class. **Top Left:** A visualisation of the t-SNE projections for digit sequences held in the test set (each point colour-coded by its label). Figure best viewed in colour.

- **VRNN-GMM:** A VRNN [30] with a GMM fit to its latent space in an isolated optimisation phase;
- **DDPAE-GMM:** The DDPAE [18] (coupled with a GMM for classification), a model that attained state-of-the-art results on Moving MNIST by disentangling and decomposing sequence representations;
- **DiSCVAE:** The proposed model of Section 3.2;
- **DiSCVAE-KLY:** A model variation where the objective $\mathcal{L}(\mathbf{x}_{\leq T})$ has the entropy measure in Eq. 10 exchanged for its respective KL divergence, *i.e.* like in Eq. 6.

In addition to these unsupervised approaches, a *supervised* bidirectional LSTM (**BiLSTM**) classifier is trained using the same CNN encoder. All models possess roughly the same network structure as specified above and are optimised over 10 runs at different random seeds until validation-based early stopping.

4.3 Results

Qualitative results of the DiSCVAE applied to the test set are demonstrated in Fig. 4. The bottom row shows the entire ground truth sequence and on the right-hand side are 10 forward sampled states from each component of the mixture prior $p(\mathbf{z}_G | y)$. For every cluster injected into the sampling procedure of Algorithm 1, the velocity characteristics of the bouncing digit are maintained yet the identity distinctly changes to match the corresponding component. Note that the trajectory just above ground truth is drawn from the inferred cluster c , *i.e.* the one maximising posterior probability (Eq. 11). Furthermore, the top left plot in Fig. 4 depicts t-SNE [50] embeddings of global latent \mathbf{z}_G , where coloured data points expose the true digit labels. This plot is generated for the best run (**90.2%** accuracy), hence the strong coherence.

Table 1 summarises classification results on the test set of Moving MNIST. Excluding the DiSCVAE, all other algorithms achieve unsatisfactory performance at deciphering digit identities from the video sequences. The VRNN-GMM combination is especially poor on account of its entangled latent representation. On the other hand, the models viewing each frame independently are marginally better due to their focus on time-invariant characteristics for reconstruction. Improvements in the DiSCVAE-KLY and DDPAE [18] with a GMM fit to its learnt “content” vector (conceptually akin to our global variable) reinforce the value of both *disentanglement* and *temporal correlations*. Nonetheless, the DiSCVAE obtains a far superior classification accuracy that is impressively comparable to the supervised BiLSTM.

Predictive performance is also exhibited in Table 1, with only the autoregressive VRNN and DDPAE models serving as baselines. The VRNN is outperformed by the DiSCVAE and DDPAE, suggesting disentangled latent attributes

Table 1: Performance on Moving MNIST test set (10 random seeds)

Model	ACC (%) \uparrow	BCE \downarrow	MSE \downarrow
SeqVAE-GMM	22.2 \pm 2.0	-	-
SeqGMVAE	18.6 \pm 1.5	-	-
VRNN-GMM	14.9 \pm 0.6	289.6 \pm 19.0	73.1 \pm 0.8
DDPAE-GMM	28.0 \pm 3.7	246.5 \pm 4.4	72.9 \pm 1.2
DiSCVAE-KLY	28.5 \pm 3.3	266.6 \pm 6.4	70.9 \pm 1.0
DiSCVAE	77.0 \pm 6.8	257.9 \pm 7.2	68.9 \pm 1.3
Superv. BiLSTM	92.59 \pm 1.64	-	-

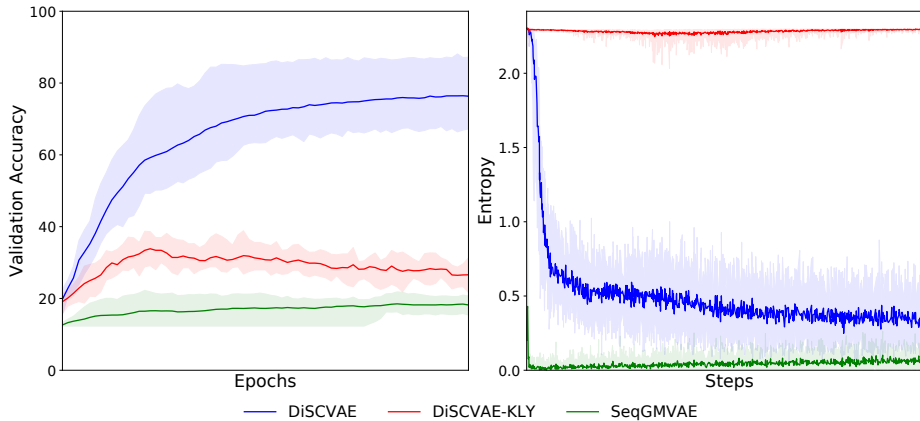


Figure 5: Validation set classification accuracy and conditional entropy of $q(y | \mathbf{x}_{\leq T})$ monitored during training runs on Moving MNIST. The model trained to minimise the KL divergence over y (DiSCVAE-KLY) exhibits cluster degeneracy, with the conditional entropy plot indicating that every observation is equally likely to be assigned to the same component. At the other extreme, the sequential GMVAE (SeqGMVAE) clearly suffers from posterior collapse. Only the entropy formulation for training a DiSCVAE yields reasonable clustering performance and a meaningful variational posterior.

can even help predict entangled future states. Between the DiSCVAE and DDPAE, the former produces better MSE scores and worse BCE measurements, indicating predictions are on average more accurate but less robust in the presence of uncertainty. The higher certainty surrounding DDPAE estimates is possibly attributed to how this model learns decomposed representations of input sequences (*e.g.* individual digits within the video), acting as an attention mechanism towards salient regions for prediction [18, 45]. Any discrepancy in DDPAE performance from the original work [18] is by virtue of a much smaller dataset encompassing single-digit sequences.

4.4 Ablation Study

Lastly, we explore the dilemmas of posterior collapse and cluster degeneracy when modelling discrete variable y . Many techniques have been applied to evade the occurrence of a zero KL divergence term, such as KL cost annealing [37] or vector-quantisation [24], yet we find maximising the entropy of $q(y | \mathbf{x}_{\leq T})$ to be a simple and sufficient solution. This has also been corroborated by other recent works [23, 36]. To justify the claim, we examined how different models and regularisation terms for $\mathcal{L}(\mathbf{x}_{\leq T})$ affect the posterior when learning with a powerful CNN decoder. In particular, we tracked the clustering accuracy metric in Eq. 12 and the conditional entropy during training runs of the DiSCVAE, DiSCVAE-KLY and SeqGMVAE models.

Fig. 5 illustrates the evolution of these measured quantities on the validation set. When including the entropy term without modelling dependencies between timesteps (SeqGMVAE), the reconstruction loss is prioritised and leads to a uniform posterior distribution that ignores latent variable y altogether (posterior collapse). On the contrary, if temporal correlations are captured but the model is optimised under KL divergence regularisation (DiSCVAE-KLY), every sequence will project to the same component and suffer from mode collapse. In turn, we appoint an entropy constraint (DiSCVAE) that encourages cluster specialisation to input observations and avoids degeneracy despite using deep

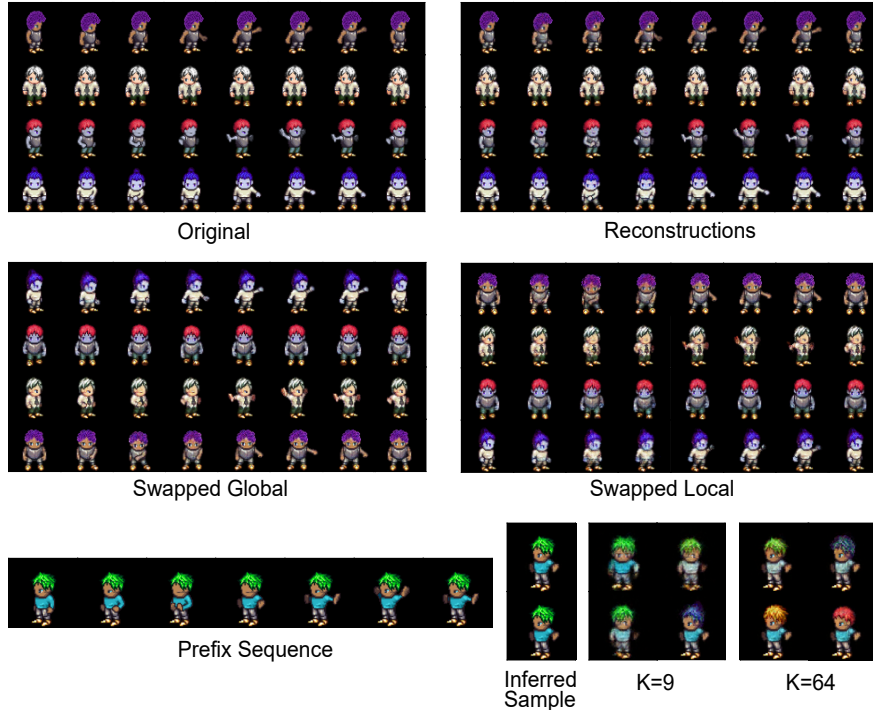


Figure 6: Visual illustrations of four “sprites” test set sequences, their DiSCVAE reconstructions, the effect of swapping global and local latent variables, and the generative capacity of different clusters. The middle row demonstrates how exchanging global \mathbf{z}_G affects the character’s attributes and swapping local $\mathbf{z}_{t,L}$ impacts their actions. The bottom row shows how last-frame predictions vary depending on K . Both K instances will infer the correct output (the bottom frame is ground truth and the inferred sample is above), however the DiSCVAE configured to $K = 9$ will draw diverse behaviours (*e.g.* turning) from its other clusters, whilst $K = 64$ samples primarily manipulate hair colour. Figure best viewed in colour.

neural networks [23, 32, 36]. Table 1 additionally shows that the DiSCVAE surpasses its KL divergence competitor in both classification and prediction.

5 Validation Setting: Sprites

This section validates the DiSCVAE in a more complex experimental setting involving the Sprites dataset [20].

5.1 Dataset and Implementation

Sprites is a synthetic dataset composed of various animated characters, *i.e.* “sprites”, which originate from an open-source video game project⁴. We use the same variant of the dataset as in [20], where there are four attribute types (skin, top, bottom and hair) and nine action categories (walking, spellcasting and slashing, each with three orientations). Every animation sequence is of length $T = 8$ frames (64×64 dimensions), and there are a total of 11664 examples, with 9000 for training and the remainder for testing. Given that each sequence possesses multiple factors of variation (*e.g.* actions, hairstyle, skin colour), Sprites is an attractive domain for disentanglement that has been explored in related works [20, 21]. See Fig. 6 for a visual illustration.

The DiSCVAE architecture and optimisation details mostly align with those chosen for Moving MNIST, with the exception of the following. First, the $\mathbf{h}_t^{\mathbf{z}_L}$ shared RNN state has 64 units. Next, each pixel is modelled as a Gaussian variable with fixed variance, represented by latents $\dim(\mathbf{z}_{t,L}) = 64$ and $\dim(\mathbf{z}_G) = 256$. Choosing K is also no longer a coherent design choice and so Section 5.3 elaborates on this matter.

⁴<https://lpc.opengameart.org/>

Table 2: Sprites test set metrics to determine K

Metric	Number of Clusters (K)						
	4	9	16	25	36	49	64
ACC \uparrow	33.3	71.4	58.6	23.3	36.5	49.7	29.7
NMI \uparrow	0.63	0.85	0.73	0.44	0.55	0.78	0.60

5.2 Evaluation Protocol

We take particular interest in classifying the action categories of individual sprites due to the resemblance with intention inference. In turn, we apply the same unsupervised classification metric defined in Eq. 12. Analogous to prior disentanglement experiments on Sprites [20, 21], we also train a k-nearest neighbour (KNN) classifier to discriminate *both* action and attribute categories from learnt latent representations. The action class has nine possible values and the four attribute types each have six values. We compute the mean average precision (mAP) individually across these five classes before taking their averaged result, as an indicator of the effectiveness of this semi-supervised approach. Predictive performance is judged by computing the MSE for last-frame predictions given the seven preceding frames.

The experiment only considers the VRNN and DDPAE from Section 4.2, as the Moving MNIST results clearly reinforced the advantages of modelling temporal correlations. We also compare against the disentangled sequential autoencoder (DSeqVAE) [20] from which the Sprites dataset originates. All models, excluding the DiSCVAE, are granted classification accuracy by fitting a GMM to their latent space in a separate training phase.

5.3 Choosing K

A crucial design choice of the DiSCVAE is to select the size of the K -dimensional action plan repertoire. Although this is straightforward for Moving MNIST, the decision is less apparent when there are many potential interpretations of classes (*e.g.* between a sprite’s action or any other attribute, like its hair colour). Fortunately, it is relatively easy to identify factors of variation from image data [8], and so the ground truth labels can aid us in this endeavour. More specifically, our aim is to create a model capable of inferring actions from sprite sequences. Therefore, two metrics are utilised to diagnose the clustering performance: unsupervised classification accuracy (ACC) and Normalised Mutual Information (NMI) across action labels. The NMI measure occupies a range of $[0, 1]$ and is unaffected by different K when assessing cluster quality. NMI has also been used amongst similar VAEs for discrete representation learning [25].

Table 2 provides the accuracy and NMI scores of the DiSCVAE trained using different K . As might have been anticipated for a 9-class category, $K = 9$ outperforms the other repertoire sizes in terms of classifying actions. Larger values of K are likely to capture a less entangled latent space and thereby be better at differentiating static qualities, such as hair colour (see Fig. 6). Nevertheless, we postulate that action inference is improved by the slightly entangled representations associated with smaller repertoire sizes. An investigation into the relationship between K and disentanglement strength (*e.g.* based on measures of informativeness, separability and interpretability [51]) is left for future work.

5.4 Results

Qualitative findings of the DiSCVAE handling four sequences from the Sprites test set are depicted in Fig. 6. The middle row presents reconstructions of these example sequences with swapped \mathbf{z}_G and $\mathbf{z}_{t,L}$, where the global and local variables exclusively manipulate caricature traits and their behaviour, respectively. The same observations were reported in the DSeqVAE paper [20], yet the DiSCVAE required a specific value of $K = 36$ to replicate this exact effect. To further expand on the relevance of K , the figure’s bottom row shows how sampled last-frame predictions are correct when drawn from the inferred cluster (top frame in grid), but exhibit different outcomes of diversity depending on K . For $K = 9$, component samples influence how the action pans out, even portraying unseen orientation turns in the first column of the grid. On the other hand, $K = 64$ components mainly control attributes, such as the sprite’s hair colour.

Table 3 summarises the quantitative results of this experiment. The DiSCVAE yields higher accuracy rates over competitive sequence disentanglement techniques, like the DDPAE and DSeqVAE, despite being completely unsupervised, *i.e.* there is no need to fit a GMM post-training. These improvements additionally transfer into the semi-supervised case, with the mAP of the k-nearest neighbour classifier trained on the DiSCVAE representations surpassing its competitors. In contrast, the MSE between last-frame prediction largely leans in favour of the VRNN, which is consistent with how *entangled* representations often yield better predictions at the expense of interpretability [15, 37]. Note that the DDPAE MSE is not reported as it was a factor of 10 higher than the rest, which we suspect is due to its

Table 3: Performance on Sprites test set (10 random seeds)

Model	ACC (%) \uparrow	mAP (%) \uparrow	MSE \downarrow
VRNN [30]	13.8 \pm 0.6	59.6 \pm 1.9	2.03 \pm 0.2
DSeqVAE [20]	62.9 \pm 6.4	81.0 \pm 3.5	4.84 \pm 0.2
DDPAE [18]	40.4 \pm 7.7	76.5 \pm 0.6	-
DiSCVAE (K=9)	73.5 \pm 4.8	88.2 \pm 3.4	2.22 \pm 0.4

nature of decomposing frames into components and modelling intra-component pose variations, rather than holistic object dynamics.

6 Intention Inference on Robotic Wheelchairs

After validating the framework’s capacity to disclose classes from sequences without supervision, we now explore intention inference in robotic wheelchair navigation. The objective here is to infer action plans of users from observations of their joystick commands and surroundings. Equipping assistive robots with an intention inference mechanism is fundamental for shared control [3], and so we also ponder the potential utility of our framework within this paradigm.

6.1 Dataset

Eight healthy subjects (aged 25-33) with experience using a robotic wheelchair were recruited to navigate three mapped environments (top right of Fig. 1). Each subject was requested to manually control the wheelchair using its joystick and follow a random route designated by goal arrows appearing on a graphical interface, as in Fig. 1. These goals are incomplete representations of human intent, as they do not reflect the action plans of subjects, *i.e.* how they act in pursuit of a goal.

Experiment data collected during trials was recorded at a rate of 10Hz, with sequences of length $T = 20$. This sequence length T is inspired by related work on estimating the short-term “local” intentions of robotic wheelchair operators [44]. Every sequence was composed of user joystick commands $\mathbf{a}_t \in \mathbb{R}^2$ (linear and angular velocities), as well as rangefinder readings $\mathbf{l}_t \in \mathbb{R}^{360}$ (1° angular resolution). Both signals perceived by the robot are synchronised to the elected system frequency as the laser sensors act as a bottleneck. The resulting dataset amounted to a total of 8883 sequences.

To experimentally assess the generalisability of our intention inference framework, we segregate the dataset according to different mapped environments. As a result, any trials that took place in Map 3 are excluded from the training and validation sets, leaving splits of 5881/1580/1422 for training/testing/validation. Dividing the dataset in this way allows us to investigate performance under variations in task context, and verify whether the DiSCVAE can elucidate human intent irrespective of such change.

6.2 Labelling Routine

Even without access to the exact, predefined labels for all possible manoeuvres of subjects while pursuing task goals, we can still appoint approximations of user “intent” to shed light on the analysis. As such, the following automated labelling routine is utilised.

Each sequence is initially categorised as either “narrow” or “wide” depending on a measure of threat applied in obstacle avoidance for indoor navigation [52]:

$$\text{threat} = \frac{1}{L} \sum_{i=1}^L \text{sat}_{[0,1]} \left(\frac{D_s + R - l_i}{D_s} \right), \quad (13)$$

where the aggregate threat score is a saturated function of L ranger readings l_i , the robot’s radius R (0.5m in the wheelchair’s case), and a safety distance parameter D_s (set to 0.8m). In essence, this score reflects the danger of imminent obstacles per timestep and qualifies narrow sequences whenever the averaged measure exceeds a certain threshold.

Next, we discern the intended navigation manoeuvres of participants from the wheelchair’s odometry. After empirically testing different thresholds for translational and angular velocity, we determined six manoeuvres: in-place rotations (left/right), forward and reverse motion, as well as forward turns (left/right). Overall, this results in 12 classes that account for the influence of both environment states and actions. Referring to Fig. 1, the majority class across

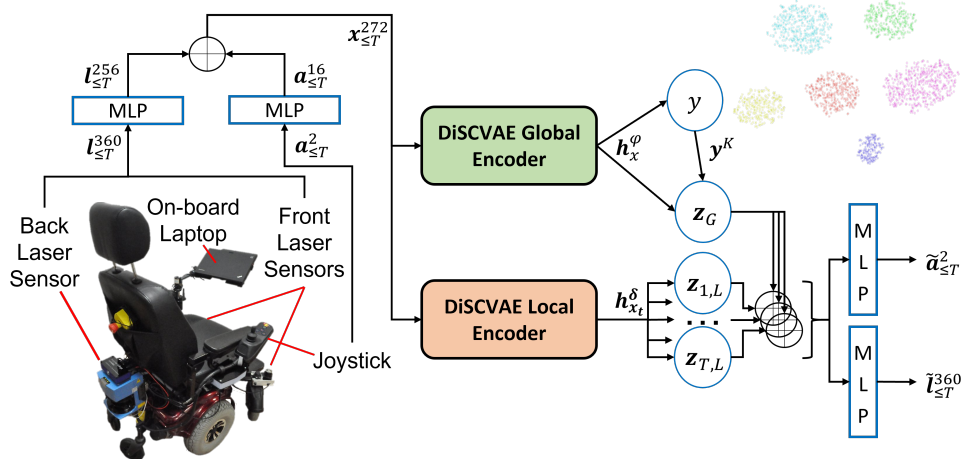


Figure 7: Network architecture for the robotic wheelchair experiment. Joystick and laser sensor data are fed into separate MLPs to produce the concatenated input sequence, $\mathbf{x}_t \in \mathbb{R}^{272}$. This sequence then feeds into the DiSCVAE encoder graph (see Fig. 3) to yield the bidirectional LSTM state \mathbf{h}_x^ϕ and hidden states $\mathbf{h}_{x_t}^\delta$ responsible for inferring variables \mathbf{z}_G and $\mathbf{z}_{t,L}$, respectively. These variables are concatenated and passed onto another set of MLPs, which decode the joystick commands $\tilde{\mathbf{a}}_t \in \mathbb{R}^2$ and rangefinder values $\tilde{\mathbf{l}}_t \in \mathbb{R}^{360}$.

Table 4: Wheelchair Validation Set metrics to determine K

Metric	Number of Clusters (K)						
	4	6	10	13	16	25	36
ELBO \uparrow	-572.2	-571.5	-569.4	-568.0	-569.2	-569.9	-570.8
NMI \uparrow	0.155	0.193	0.214	0.264	0.243	0.227	0.232

Maps 1 & 2 is the wide in-place rotation (left *and* right), whilst for Map 3 it is the narrow reverse. This switch in label frequency highlights the task diversity resulting from different maps.

6.3 Implementation

The mobile platform is a powered wheelchair enhanced with an on-board computer and three laser sensors, two at the front and one at the back for full 360° field of view. For readers interested in the robot architecture, please refer to our earlier work on shared control [53, 54].

A complete network architecture for this experiment is portrayed in Fig. 7 and mimics the graphical model of Fig. 3, excluding the extra steps to process two input modalities. The raw laser vector $\mathbf{l}_{\le T}$ and 2D user control commands $\mathbf{a}_{\le T}$ are first passed through separate single-layer MLPs with 512 units (ReLU activations). The derived code vectors are then concatenated together to yield $\mathbf{x}_{\le T}$, which is fed into the DiSCVAE to infer latent variables \mathbf{z}_G and $\mathbf{z}_{\le T,L}$. Two individual decoders are conditioned on these variables and trained to reconstruct the original input modalities. Note that odometry data is not supplied to this network.

The following describes noteworthy model or training differences over our earlier experiments. Sensory observations are modelled as Gaussian variables with fixed variance. Sequences are normalised per modality before entering the network using the mean and standard deviation of the training set, as in preceding sequential VAE models [28]. Latent variables representing observed data have dimensions $\dim(\mathbf{z}_G) = \phi = 16$ and $\dim(\mathbf{z}_{t,L}) = \delta = 16$. The Adam optimiser [46] is configured with a 1×10^{-3} learning rate and parameter selection relied on the validation set, as well as common choices from the relevant literature [8].

Regarding the selection of K , a similar procedure to the one in Sprites was employed. The lack of access to ground truth factors of variation means an unsupervised metric, namely the ELBO, was utilised instead of Eq. 12. Table 4 provides the ELBO and NMI for different K in the range 4-36. We settled on $K = 13$ due to its marginal superiority and resemblance to the class count from Section 6.2.

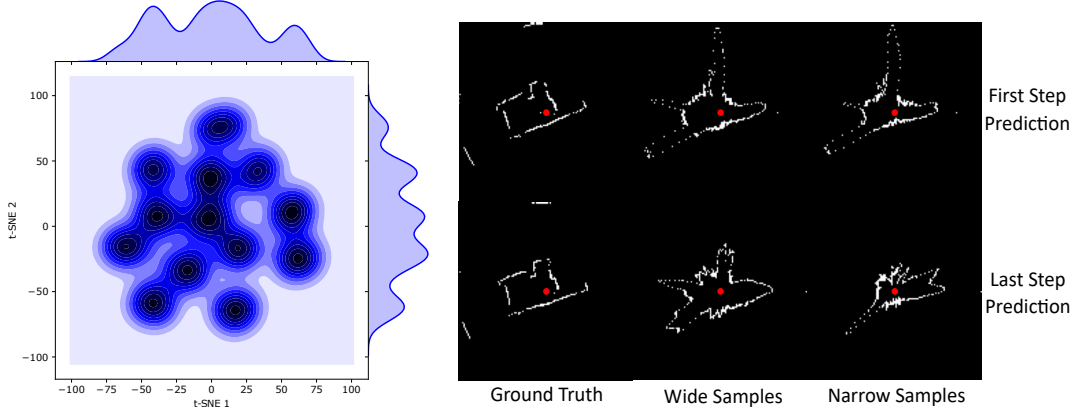


Figure 8: **Left:** t-SNE embeddings of component samples drawn from a $K = 13$ mixture prior. The joint density plot illustrates how a multimodal latent space is learnt from the robotic wheelchair data, with separable clusters representing intent. **Right:** 2D grids of predicted laser scans on the test set when sampling from “wide” and “narrow” type clusters. Wide samples create spacious proximity around the wheelchair (red dot), whilst narrow samples enclose space.

6.4 Evaluation

Although there are no actual labels available in most practical settings, including ours, we are still interested in digesting the prospects of the DiSCVAE for downstream tasks, such as semi-supervised classification. As in Sprites, we train a KNN classifier over the learnt latent representation, \mathbf{z}_G , and judge classification performance using standard intention estimation metrics of accuracy and the F1-score [7, 55]. Another typical error measure in the field is mean squared error (MSE) [7, 10], hence we compare the trajectory predictions of user actions $\hat{\mathbf{a}}_t$ and laser readings $\hat{\mathbf{l}}_t$ for 10 forward sampled states against “ground truth” future states.

For this experiment, the following methods are considered:

- **HMM:** A baseline that is ubiquitous in the human intention inference literature [5, 10];
- **SeqSVM:** A sequential Support Vector Machine (SVM) baseline [7, 9];
- **BiLSTM:** A bidirectional LSTM classifier, akin to other LSTM architectures for intention estimation [55];
- **VRNN:** The same popular autoregressive VAE model that has previously been tested [30];
- **DiSCVAE:** The proposed model of Section 3.2.

The top three models learn mappings between inputs and the labels identified in Section 6.2 in a *supervised* fashion. Meanwhile, the VRNN [30] and DiSCVAE optimise their respective ELBOs, with a KNN trained on their learnt latent variables for a *semi-supervised* approach. All deep neural networks maintain the same encoder structure as in Fig. 7.

6.5 Results

In terms of qualitative analysis, we show how action and state samples emerge from the prior latent space of the DiSCVAE. Fig. 1 portrays forecasted trajectories by sampling from each mixture component during a subject’s recorded interaction. There is clear variability in the trajectory outcomes predicted for this specific wheelchair configuration ($K = 6$ to ease visualisation). The plotted categorical probability histogram (top left of Fig. 1) also indicates that the most probable trajectory aligns with the wheelchair user’s current goal (red arrow), *i.e.* the correct “intention”. As for generating future environment states, Fig. 8-Right displays how samples from clusters manifest when categorised as either “wide” or “narrow”. Meanwhile, Fig. 8-Left depicts how random component samples from a $K = 13$ mixture prior form distinguishable clusters and reveal a multimodal latent space.

Table 5 demonstrates the quantitative results for this experiment. As anticipated, the highly variable nature of wheelchair control in an unconstrained navigation task makes classifying intent extremely challenging. Even the supervised BiLSTM obtains a classification rate of merely 53.3% on the unseen test environment. Nevertheless, learning representations of intent can clearly garner benefits in inference, as the accuracy rates are drastically improved by training a simple classifier over the latent space of the DiSCVAE and VRNN. MSE scores for trajectory prediction of joystick and ranger values show that the DiSCVAE and VRNN are alike in their error estimates.

Table 5: Performance on Wheelchair Test Set (10 random seeds)

Model	Acc (%) \uparrow	F1 \uparrow	$\tilde{\mathbf{a}}_{MSE} \downarrow$	$\tilde{\mathbf{I}}_{MSE} \downarrow$
HMM	13.5 \pm 0.9	0.06 \pm 0.01	-	-
SeqSVM	42.9 \pm 0.1	0.28 \pm 0.00	-	-
BiLSTM	53.3 \pm 2.5	0.37 \pm 0.02	-	-
VRNN	65.0 \pm 0.9	0.61 \pm 0.01	0.18 \pm 0.02	3.16 \pm 0.07
DiSCVAE	83.2 \pm 0.6	0.78 \pm 0.01	0.18 \pm 0.01	3.15 \pm 0.05

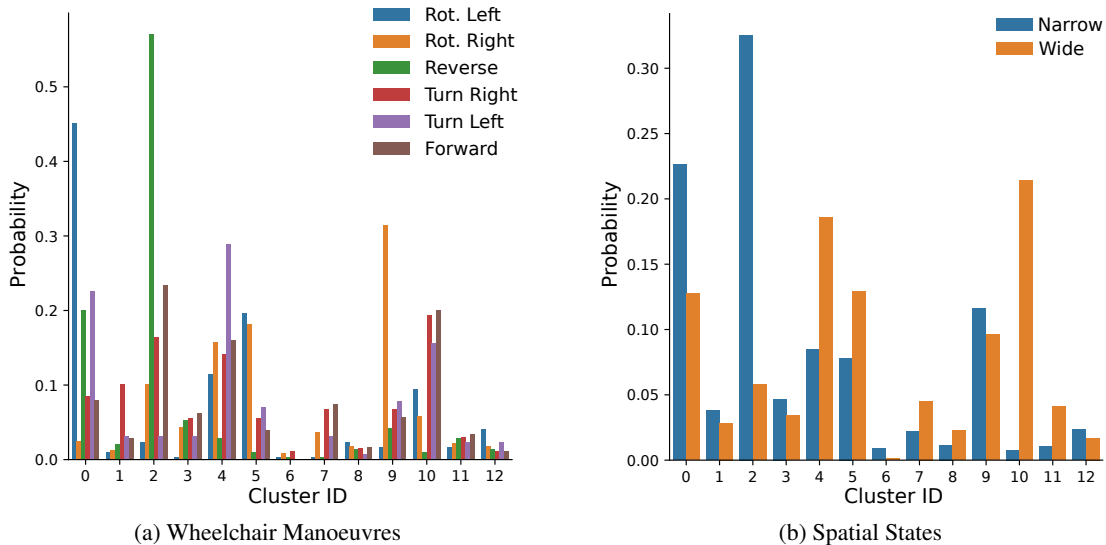


Figure 9: Assignment distribution of y for $K = 13$ with post-processed labels for **(a)** wheelchair manoeuvres and **(b)** perceived spatial context. The plot illuminates how various clusters are associated with user intent under different environmental conditions. For example, most backward motion and “narrow” state samples reside in cluster 2. Similar patterns are noticeable for in-place rotations (0 and 9) and “wide” forward motion (4 and 10).

Three important conclusions can be drawn from these results. Principally, relying on accuracy metrics for evaluation is not necessarily informative on the underlying distribution of intent. Instead interpretability is germane to the evaluation [8], in which the DiSCVAE substantially gains as a transparent clustering model of human intent (elaborated on in Section 6.6). Second, the elevated classification performance posits that semi-supervised learning is a worthwhile avenue to explore in future applications, especially in user modelling on larger interaction datasets. Lastly, the time-invariant and time-varying elements of wheelchair navigation are possibly interdependent, as reinforced by the balanced dimensionality of local and global features.

6.6 Illuminating the Clusters

Straying away from the purely discriminative task of classifying intent, we now use our framework to decipher the “local” wheelchair navigation behaviours intended by users. In particular, we plot the assignment distributions of y for each test set example in the dataset to understand the underlying meaning of our clustered latent space.

Fig. 9a provides further clarity on how certain clusters have learnt independent wheelchair manoeuvres. For instance, cluster 2 is distinctly linked with the wheelchair’s reverse motion. Likewise, clusters 0 and 9 are affiliated with left and right in-place rotations. The spatial state assignments shown in Fig. 9b also delineate how these listed clusters are most often categorised as “narrow”. This result is to be expected of evasive actions that habitually take place in cluttered spaces. On the contrary, predominantly forward-oriented manoeuvres fall into “wide” clusters (e.g. 4 and 10). These findings corroborate that an action plan repertoire has been aptly inferred using our proposed framework.

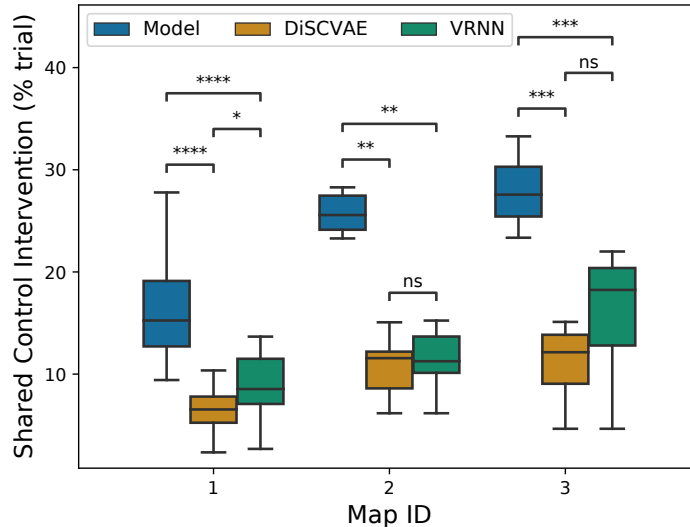


Figure 10: Percentage of trials where shared control would have wrongly intervened across the three maps. The Model approach of predicting wheelchair trajectories is significantly more likely to trigger incorrect assistance. There is also less variability in the VRNN and DiSCVAE performance across different maps, suggesting better robustness to changes in task conditions.

6.7 Prospects for Shared Control

Finally, we examine a use-case of our framework within shared control, where intention inference plays a vital role [3]. Shared control concerns the interaction between robots and humans when *both* exert control over a system to accomplish a common goal [4]. Despite shared control being inactive for this experiment, we imitate its operation in post-processing to gauge success.

More specifically, we address the known issue in shared control of providing *wrong* assistance whenever there is a misalignment between the robot’s and user’s internal models. To quantify this mismatch, we monitor the percentage of each navigation trial where a shared control methodology [54] would have arbitrated user input had it been operational. Given how each subject is an experienced, healthy individual that incurred no wheelchair collisions, it is safe to assume they never required assistance. We compare one-second simulations of wheelchair trajectories produced by the VRNN, DiSCVAE, and a constant-velocity “Model” that projects states using differential drive kinematics.

Fig. 10 summarises the results on shared control intervention rates. Performing the two-sided Mann-Whitney U test finds statistically significant better rates garnered by the VAE-based algorithms over the Model across all maps ($p \leq 0.01$). Excluding Map 1 ($p \leq 0.05$), the positive trend of the DiSCVAE surpassing the VRNN is not significant. However, human intent inferred via the DiSCVAE is visually representable (*e.g.* Figs. 1 and 9), which may hold immense potential for shared control seeking to realign mismatched internal models through explanation [53, 54].

7 Related Work

Sequence Disentanglement Our work builds on the VAE paradigm [12, 13] and its sequential extensions [28–31] in uncovering general priors about real-world data [14]. In order to derive these priors for human intent, we advocate against heavily relying on access to predefined labels of desire. Consequently, most supervised techniques are deemed inappropriate, unless they exploit a partial dependency (*e.g.* semi-supervised and few-shot learning [15, 16]). By removing the notion of ground truth in favour of a task-agnostic prior, we divert our focus from classifying to *disentangling* intent.

A considerable number of sequential frameworks involving VAEs have enjoyed success at learning disentangled representations. In video data, numerous models have employed the strategy of using separate encoders to isolate motion and content features [17, 19]. Other video prediction models have utilised the same strategy, but additionally applied decomposition [18], attention [45] or more complex model priors [21] to further compartmentalise these features into *multiple* factors of variation. Partitioning the latent space into time-invariant and time-dependent subsets can also serve other sequential data, *e.g.* text and speech [20, 23].

Interpretable Representation Learning An integral asset of disentangled representations lies in their *interpretability* [8]. The capacity to interpret latent spaces can facilitate abstract reasoning for practical outcomes, such as counting bouncing digits from video sequences [45] or determining a patient’s mortality risk based on their medical records [25]. One prominent form of disentanglement that enhances the level of interpretability is to incorporate discrete information into the latent variable model [24].

An exemplification of how discrete latent codes can augment a model’s interpretability is through *clustering*. In VAEs, temporal clustering has previously been achieved by either directly manipulating the latent manifold into a discrete format [25] or inferring categorical attributes to compose mixture priors [23, 36]. Although clustered priors enable the diagnosis of learnt representations, careful parameter tuning [8] and clever objective loss terms [36, 40] are required to avoid a collapsing latent space. Whilst clustering models complementary to ours have addressed this matter [23, 36], a notable difference in our DiSCVAE is that it employs a mixture prior to cluster over *only* the global part of its disentangled representation, \mathbf{z}_G , rather than the entirety of an entangled one. As a result, we choose an inductive bias that separates continuous action dynamics from discrete higher-level goals when comprehending human intent [2].

Intention Estimation The general problem of intention understanding essentially revolves around an observing agent deriving a model to match an acting agent’s behaviour [3]. In human-robot interaction, this problem is typically addressed by equipping an observing robot with a probabilistic model that infers intent from human actions [5–7]. The growing interest in scalable learning techniques for modelling agent intent has also spurred on applications in robotics for purposes like shared control [55–57] and multi-agent governance [58]. However, disentangled learning remains sparse in the literature, with the only known comparable work to ours being a conditional VAE that disentangled latent variables in a multi-agent driving setting [11]. Albeit similar in principle, we believe our approach is the first to infer a discrete “intent” variable from human behaviour by clustering action plans.

8 Conclusions

In this work, we embraced a novel outlook on human intention inference and introduced a deep generative model to simultaneously disentangle and cluster sequence representations. The overall framework is broadly applicable to sequential data, as proven by revealing classes from synthetic video sequences of bouncing digits and 2D animations. A robotic wheelchair experiment on intention inference also gleaned insights into how our model could discern primitive action plans from observations, *e.g.* rotating in-place or reversing. We believe these contributions can equally serve the machine learning and robotics communities.

There are numerous promising research avenues for an unsupervised means of inferring intent in human-robot interaction. For instance, the task-agnostic prior could be exploited in downstream tasks, such as user modelling, to augment the wider adoption of collaborative robotics in unconstrained environments. Our findings on semi-supervised learning from the robotic wheelchair experiment fortify this idea. The interpretable latent structure could also prove fruitful in assistive robots that warrant explanation by visually relaying inferred intentions back to end-users [53, 54]. A final course of inquiry could be to incorporate these explanations into an interactive learning procedure [8], *e.g.* for user personalisation.

Acknowledgements

This research was supported by an EPSRC Doctoral Training Award to Mark Zolotas and a Royal Academy of Engineering Chair in Emerging Technologies to Yiannis Demiris.

References

- [1] S J Blakemore and J Decety. From the perception of action to the understanding of intention. *Nature Reviews Neuroscience*, 2(8):561–567, 2001.
- [2] Michael Tomasello, Malinda Carpenter, Josep Call, Tanya Behne, and Henrike Moll. Understanding and sharing intentions: The origins of cultural cognition. *Behavioral and Brain Sciences*, 28(5):675–691, 2005.
- [3] Yiannis Demiris. Prediction of intent in robotics and multi-agent systems. *Cognitive Processing*, 8(3):151–158, 2007.
- [4] Dylan P. Losey, Craig G. McDonald, Edoardo Battaglia, and Marcia K. O’Malley. A review of intent detection, arbitration, and communication aspects of shared control for physical human-robot interaction. *Applied Mechanics Reviews*, 70(1), 2018.

- [5] Siddharth Jain and Brenna Argall. Probabilistic Human Intent Recognition for Shared Autonomy in Assistive Robotics. *Journal of Human-Robot Interaction*, 9(1), 2019.
- [6] Shervin Javdani, Siddhartha S Srinivasa, and J Andrew Bagnell. Shared autonomy via hindsight optimization. *Robotics science and systems: online proceedings*, 2015.
- [7] Y Hu, W Zhan, and M Tomizuka. Probabilistic Prediction of Vehicle Semantic Intention and Motion. In *IEEE Intelligent Vehicles Symposium*, pages 307–313, 2018.
- [8] Francesco Locatello, Stefan Bauer, Mario Lucic, Gunnar Raetsch, Sylvain Gelly, Bernhard Schölkopf, and Olivier Bachem. Challenging common assumptions in the unsupervised learning of disentangled representations. In *International Conference on Machine Learning*, pages 4114–4124, 2019.
- [9] Zhikun Wang, Katharina Mülling, Marc Peter Deisenroth, Heni Ben Amor, David Vogt, Bernhard Schölkopf, and Jan Peters. Probabilistic movement modeling for intention inference in human-robot interaction. *The International Journal of Robotics Research*, 32(7):841–858, 2013.
- [10] A K Tanwani and S Calinon. A generative model for intention recognition and manipulation assistance in teleoperation. In *IEEE/RSJ International Conference on Intelligent Robots and Systems*, pages 43–50, 2017.
- [11] Y Hu, W Zhan, L Sun, and M Tomizuka. Multi-modal Probabilistic Prediction of Interactive Behavior via an Interpretable Model. In *IEEE Intelligent Vehicles Symposium*, pages 557–563, 2019.
- [12] Diederik P Kingma and Max Welling. Auto-Encoding Variational Bayes. *arXiv preprint arXiv:1312.6114*, 2013.
- [13] Danilo Jimenez Rezende, Shakir Mohamed, and Daan Wierstra. Stochastic Backpropagation and Approximate Inference in Deep Generative Models. In *International Conference on Machine Learning*, pages 1278–1286, 2014.
- [14] Yoshua Bengio, Aaron Courville, and Pascal Vincent. Representation learning: A review and new perspectives. *IEEE Transactions on Pattern Analysis and Machine Intelligence*, 35(8):1798–1828, 2013.
- [15] Michael Tschannen, Olivier Bachem, and Mario Lucic. Recent advances in autoencoder-based representation learning. *arXiv preprint arXiv:1812.05069*, 2018.
- [16] Durk P Kingma, Shakir Mohamed, Danilo Jimenez Rezende, and Max Welling. Semi-supervised Learning with Deep Generative Models. In *Advances in Neural Information Processing Systems*, pages 3581–3589, 2014.
- [17] Emily L Denton and vighnesh Birodkar. Unsupervised learning of disentangled representations from video. In *Advances in Neural Information Processing Systems*, volume 30, pages 4414–4423, 2017.
- [18] Jun-Ting Hsieh, Bingbin Liu, De-An Huang, Li F Fei-Fei, and Juan Carlos Niebles. Learning to Decompose and Disentangle Representations for Video Prediction. In *Advances in Neural Information Processing Systems*, pages 517–526, 2018.
- [19] Ruben Villegas, Jimei Yang, Seunghoon Hong, Xunyu Lin, and Honglak Lee. Decomposing motion and content for natural video sequence prediction. *arXiv preprint arXiv:1706.08033*, 2018.
- [20] Li Yingzhen and Stephan Mandt. Disentangled Sequential Autoencoder. In *International Conference on Machine Learning*, pages 5670–5679, 2018.
- [21] Sarthak Bhagat, Shagun Uppal, Zhuyun Yin, and Nengli Lim. Disentangling multiple features in video sequences using gaussian processes in variational autoencoders. In *European Conference on Computer Vision*, pages 102–117, 2020.
- [22] Wei-Ning Hsu, Yu Zhang, and James Glass. Unsupervised Learning of Disentangled and Interpretable Representations from Sequential Data. In *Advances in Neural Information Processing Systems*, pages 1878–1889, 2017.
- [23] Wei-Ning Hsu, Yu Zhang, Ron J Weiss, Heiga Zen, Yonghui Wu, Yuxuan Wang, Yuan Cao, Ye Jia, Zhifeng Chen, Jonathan Shen, et al. Hierarchical generative modeling for controllable speech synthesis. *arXiv preprint arXiv:1810.07217*, 2018.
- [24] Aaron van den Oord, Oriol Vinyals, and Koray Kavukcuoglu. Neural Discrete Representation Learning. In *Advances in Neural Information Processing Systems*, pages 6306–6315, 2017.
- [25] Vincent Fortuin, Matthias Hüser, Francesco Locatello, Heiko Strathmann, and Gunnar Rätsch. Som-vae: Interpretable discrete representation learning on time series. *arXiv preprint arXiv:1806.02199*, 2018.
- [26] Nitish Srivastava, Elman Mansimov, and Ruslan Salakhutdinov. Unsupervised Learning of Video Representations Using LSTMs. In *International Conference on Machine Learning*, pages 843–852, 2015.
- [27] C Zhang, J Bütepage, H Kjellström, and S Mandt. Advances in Variational Inference. *IEEE Transactions on Pattern Analysis and Machine Intelligence*, 41(8):2008–2026, 2019.

- [28] Marco Fraccaro, Søren Kaae Sønderby, Ulrich Paquet, and Ole Winther. Sequential neural models with stochastic layers. *Advances in Neural Information Processing Systems*, 29:2199–2207, 2016.
- [29] Rahul G Krishnan, Uri Shalit, and David Sontag. Structured Inference Networks for Nonlinear State Space Models. In *AAAI Conference on Artificial Intelligence*, pages 2101–2109, 2017.
- [30] Junyoung Chung, Kyle Kastner, Laurent Dinh, Kratarth Goel, Aaron C Courville, and Yoshua Bengio. A Recurrent Latent Variable Model for Sequential Data. In *Advances in Neural Information Processing Systems*, pages 2980–2988, 2015.
- [31] Anirudh Goyal, Alessandro Sordoni, Marc-Alexandre Côté, Nan Rosemary Ke, and Yoshua Bengio. Z-forcing: Training stochastic recurrent networks. In *Advances in Neural Information Processing Systems*, pages 6713–6723, 2017.
- [32] Nat Dilokthanakul, Pedro AM Mediano, Marta Garnelo, Matthew CH Lee, Hugh Salimbeni, Kai Arulkumaran, and Murray Shanahan. Deep unsupervised clustering with gaussian mixture variational autoencoders. *arXiv preprint arXiv:1611.02648*, 2016.
- [33] Zhuxi Jiang, Yin Zheng, Huachun Tan, Bangsheng Tang, and Hanning Zhou. Variational Deep Embedding: An Unsupervised and Generative Approach to Clustering. In *International Joint Conference on Artificial Intelligence*, pages 1965–1972, 2017.
- [34] Chris J Maddison, Andriy Mnih, and Yee Whye Teh. The concrete distribution: A continuous relaxation of discrete random variables. *arXiv preprint arXiv:1611.00712*, 2016.
- [35] Eric Jang, Shixiang Gu, and Ben Poole. Categorical reparameterization with gumbel-softmax. *arXiv preprint arXiv:1611.01144*, 2016.
- [36] Wenxian Shi, Hao Zhou, Ning Miao, and Lei Li. Dispersed EM-VAEs for Interpretable Text Generation. In *International Conference on Machine Learning*, pages 5982–5992, 2020.
- [37] Irina Higgins, Loïc Matthey, Arka Pal, Christopher Burgess, Xavier Glorot, Matthew M Botvinick, Shakir Mohamed, and Alexander Lerchner. beta-vae: Learning basic visual concepts with a constrained variational framework. *International Conference on Learning Representations*, 2017.
- [38] Matthew D Hoffman and Matthew J Johnson. Elbo surgery: yet another way to carve up the variational evidence lower bound. In *Workshop in Advances in Approximate Bayesian Inference, NIPS*, volume 1, page 2, 2016.
- [39] Emilien Dupont. Learning Disentangled Joint Continuous and Discrete Representations. In *Advances in Neural Information Processing Systems*, pages 710–720, 2018.
- [40] Emile Mathieu, Tom Rainforth, N Siddharth, and Yee Whye Teh. Disentangling disentanglement in variational autoencoders. In *International Conference on Machine Learning*, pages 4402–4412, 2019.
- [41] Alex Graves and Jürgen Schmidhuber. Framewise phoneme classification with bidirectional LSTM and other neural network architectures. *Neural Networks*, 18(5):602–610, 2005.
- [42] Sepp Hochreiter and Jürgen Schmidhuber. Long Short-Term Memory. *Neural Computation*, 9(8):1735–1780, 1997.
- [43] T Carlson and Y Demiris. Collaborative Control for a Robotic Wheelchair: Evaluation of Performance, Attention, and Workload. *IEEE Transactions on Systems, Man, and Cybernetics, Part B (Cybernetics)*, 42(3):876–888, 2012.
- [44] J Poon, Y Cui, J V Miro, T Matsubara, and K Sugimoto. Local driving assistance from demonstration for mobility aids. In *IEEE International Conference on Robotics and Automation*, pages 5935–5941, 2017.
- [45] Adam Kosiorok, Hyunjik Kim, Yee Whye Teh, and Ingmar Posner. Sequential attend, infer, repeat: Generative modelling of moving objects. *Advances in Neural Information Processing Systems*, 31:8606–8616, 2018.
- [46] Diederik P. Kingma and Jimmy Ba. Adam: A Method for Stochastic Optimization. *arXiv preprint arXiv:1412.6980*, 2014.
- [47] Martín Abadi, Paul Barham, Jianmin Chen, Zhifeng Chen, Andy Davis, Jeffrey Dean, Matthieu Devin, Sanjay Ghemawat, Geoffrey Irving, Michael Isard, et al. Tensorflow: A system for large-scale machine learning. In *USENIX Symposium on Operating Systems Design and Implementation*, pages 265–283, 2016.
- [48] Joshua V Dillon, Ian Langmore, Dustin Tran, Eugene Brevdo, Srinivas Vasudevan, Dave Moore, Brian Patton, Alex Alemi, Matt Hoffman, and Rif A Saurous. Tensorflow distributions. *arXiv preprint arXiv:1711.10604*, 2017.
- [49] Harold W Kuhn. The hungarian method for the assignment problem. *Naval research logistics quarterly*, 2(1-2):83–97, 1955.

- [50] Laurens van der Maaten and Geoffrey Hinton. Visualizing data using t-sne. *Journal of machine learning research*, 9:2579–2605, 2008.
- [51] Kien Do and Truyen Tran. Theory and evaluation metrics for learning disentangled representations. *arXiv preprint arXiv:1908.09961*, 2019.
- [52] J W Durham and F Bullo. Smooth Nearness-Diagram Navigation. In *IEEE/RSJ International Conference on Intelligent Robots and Systems*, pages 690–695, 2008.
- [53] Mark Zolotas, Joshua Elsdon, and Yiannis Demiris. Head-mounted augmented reality for explainable robotic wheelchair assistance. In *IEEE/RSJ International Conference on Intelligent Robots and Systems*, pages 1823–1829, 2018.
- [54] M Zolotas and Y Demiris. Towards Explainable Shared Control using Augmented Reality. In *IEEE/RSJ International Conference on Intelligent Robots and Systems*, pages 3020–3026, 2019.
- [55] D Nicolis, A M Zanchettin, and P Rocco. Human intention estimation based on neural networks for enhanced collaboration with robots. In *IEEE/RSJ International Conference on Intelligent Robots and Systems*, pages 1326–1333, 2018.
- [56] Siddharth Reddy, Anca D Dragan, and Sergey Levine. Shared autonomy via deep reinforcement learning. *arXiv preprint arXiv:1802.01744*, 2018.
- [57] Dylan P Losey, Krishnan Srinivasan, Ajay Mandlekar, Animesh Garg, and Dorsa Sadigh. Controlling Assistive Robots with Learned Latent Actions. *arXiv preprint arXiv:1909.09674*, 2019.
- [58] Annie Xie, Dylan P Losey, Ryan Tolsma, Chelsea Finn, and Dorsa Sadigh. Learning Latent Representations to Influence Multi-Agent Interaction. *arXiv preprint arXiv:2011.06619*, 2020.